Catalytic function of zinc finger proteins against amyloid-β amyloidogenesis

Seongmin Park[1], Yunha Hwang[2], Yuxi Lin[3], Jimin Kwak[1], Eunju Nam[1], Jiyeon Han[1,4], Hyun Goo Kang[5], Jiyong Park[1,6]*, Young-Ho Lee[3,7,8,9,10]*, Seung Jae Lee[2,11]* and Mi Hee Lim[1]*

[1]Department of Chemistry, Korea Advanced Institute of Science and Technology (KAIST), Daejeon 34141, Republic of Korea

[2]Department of Chemistry, Jeonbuk National University, Jeonju 54896, Republic of Korea

[3]Biopharmaceutical Research Center, Korea Basic Science Institute (KBSI), Ochang 28119, Republic of Korea

[4]Department of Applied Chemistry, University of Seoul, Seoul 02504, Republic of Korea

[5]Department of Neurology and Research Institute of Clinical Medicine, Jeonbuk National University Hospital, Jeonju 54896, Republic of Korea

[6]Center for Catalytic Hydrocarbon Functionalizations, Institute for Basic Science (IBS), Daejeon 34141, Republic of Korea

[7]Bio-Analytical Science, University of Science and Technology (UST), Daejeon 34113, Republic of Korea

[8]Graduate School of Analytical Science and Technology, Chungnam National University, Daejeon 34134, Republic of Korea

[9]Department of Systems Biotechnology, Chung-Ang University (CAU), Gyeonggi 17546, Republic of Korea

[10]Frontier Research Institute for Interdisciplinary Sciences (FRIS), Tohoku University, Sendai, Miyagi 980-8578, Japan

[11]Institute of Molecular Biology and Genetics, Jeonbuk National University, Jeonju 54896, Republic of Korea

*To whom correspondence should be addressed: miheelim@kaist.ac.kr, slee026@jbnu.ac.kr, mr0505@kbsi.re.kr, and jiyongpa@ibs.re.kr

Graphical abstract

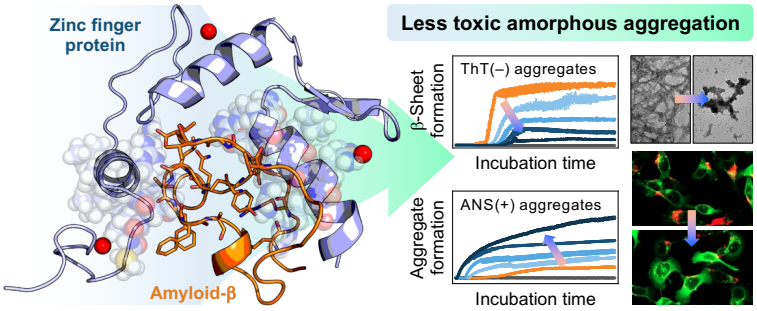

Abstract

Zinc finger (ZF) proteins are integral to neurological processes by mediating biomolecular interactions and regulating gene expression. Despite their implication in neurodegenerative diseases, the precise contribution of ZF proteins to disease pathology remains unclear. Here we show the direct binding of the ZF protein PARIS(ZF2–4) with amyloid-β (Aβ) as well as its catalytic function in reprofiling Aβ aggregation and cytotoxicity, a key contributor to Alzheimer's disease. The complex formation between PARIS(ZF2–4) and Aβ promotes the amorphous aggregation of Aβ, which reduces its interaction with cell membranes and prevents the formation of toxic oligomers and fibrils, thus alleviating Aβ-induced cytotoxicity. Through sequence-based reactivity and mechanistic analyses employing fragments and variants, we identify structural motifs critical for PARIS(ZF2–4)'s function. These findings demonstrate a novel modulative role of ZF proteins in Aβ amyloidogenesis, highlighting a sequence–reactivity relationship that offers insights into potential therapeutic avenues for neurodegenerative disorders.

Zinc finger (ZF) proteins, key members of the metalloprotein family utilizing zinc as a structural cofactor, play essential roles in orchestrating various biological processes in the brain[1-4]. These proteins are intricately involved in genetic regulation, governing complex neurological functions, including neurodevelopment, neuroprotection against oxidative stress, and the modulation of learning and memory[2,5-7]. By interacting with a diverse range of biomolecules, including DNA, RNA, lipids, and proteins, ZF proteins finely tune transcriptional and translational processes[4,8-11]. Thus, strategic manipulation of ZF proteins through rational engineering shows promise for reshaping neurological pathways[2,10,12]. When these proteins are dysregulated, however, they have been linked to neurodegenerative disorders, such as Alzheimer's disease (AD), which is characterized by progressive memory and cognitive decline[5-7,13].

Parkin-interacting substrate (PARIS; ZNF746) is a ZF protein that contains one non-classical $Cys_2HisCys$ and three classical Cys_2His_2 ZF domains in the *C*-terminal region, as depicted in Fig. 1a[14,15]. Under normal intracellular conditions, PARIS is regulated by the ubiquitin-proteasome system *via* its binding to an E3 ubiquitin ligase, Parkin, which leads to its ubiquitination and serves as a mechanism for PARIS control[14,15]. PARIS regulates gene expression by binding to insulin-response sequences within the promoter region of peroxisome proliferator-activated receptor gamma coactivator-1α (PGC-1α), an essential mediator of cellular remodeling and the expression of reactive oxygen species-detoxifying enzymes[14-17]. Thus, PARIS functions as a transcriptional regulator of PGC-1α expression. Recent research highlights potential pathogenic implications of PARIS accumulation following Parkin inactivation, resulting in mitochondrial dysfunction and increased oxidative stress through the downregulation of PGC-1α expression[14-16].

PARIS(ZF2–4), crucial for PARIS's binding to Parkin and PGC-1α[14,16], comprises three classical Cys_2His_2 ZF structural motifs (Fig. 1a), possessing the capacities to bind to diverse proteins and possibly influence multiple neurological processes, including those relevant to diseased states[2,6,7,11,15,18]. Thus, we questioned the expanded functional role of the ZF structural domains of PARIS in interacting with amyloidogenic proteins and altering their aggregation dynamics and cytotoxicity, central to the pathogenesis of neurodegenerative disorders[13]. Among the plethora of amyloidogenic proteins, amyloid-β (Aβ) peptides have drawn particular attention due to their co-localization with Parkin, upregulation under Parkin-inactivated conditions, and deposition in AD-affected brains[13,19,20]. Aβ peptides tend to self-assemble into oligomers, protofibrils, and fibrils, each contributing to the pathological cascade (Fig. 1b)[20-23]. Particularly, soluble and structured oligomers are toxic, causing cellular damage through multiple mechanisms,

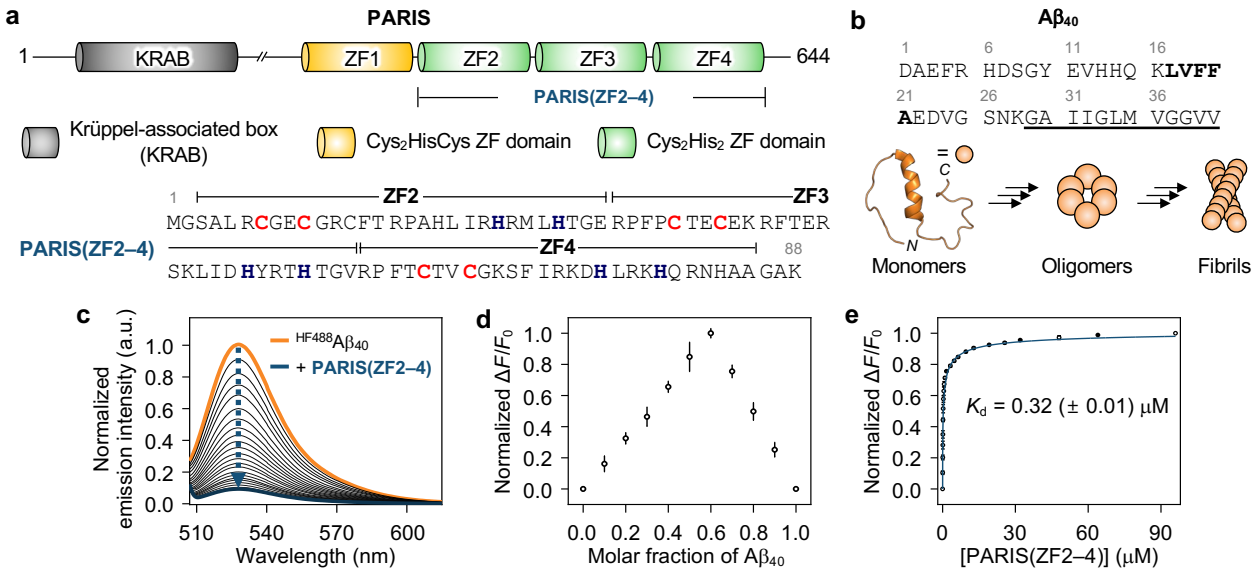

Fig. 1 | PARIS(ZF2–4) and Aβ studied in this work. a, Domain organization of PARIS with the amino acid sequence of its classical ZF segments [PARIS(ZF2–4)]. The cysteine and histidine residues involved in Zn(II) coordination are highlighted in bold red and navy, respectively. **b,** Amino acid sequence and aggregation of $A\beta_{40}$. A partially folded $A\beta_{40}$ (PDB 2LFM[43]) determined by NMR spectroscopy is depicted as a representative monomeric structure under aqueous conditions. Amino acid residues involved in the self-recognition and *C*-terminal hydrophobic regions are indicated in bold and underline, respectively. **c–e,** Binding properties of PARIS(ZF2–4) [$Zn(II)_3$-bound form] towards $A\beta_{40}$ measured by fluorescence-based quenching experiments. The change in intrinsic $^{HF488}A\beta_{40}$ fluorescence was traced upon titrating various concentrations of PARIS(ZF2–4). The K_d value for the PARIS(ZF2–4)–$A\beta_{40}$ adduct was determined by fitting the $\Delta F/F_0$ values based on their binding stoichiometry estimated by Job plot. Conditions: (for fluorescence quenching studies) [$^{HF488}A\beta_{40}$] = 320 nM; [PARIS(ZF2–4)] = 0 to 96 μM; 20 mM HEPES, pH 7.4, 1 mM DTT; room temperature; λ_{ex} = 503 nm; λ_{em} = 507–675 nm; (for Job plot measurements) [$^{HF488}A\beta_{40}$] + [PARIS(ZF2–4)] = 640 nM; 20 mM HEPES, pH 7.4, 1 mM DTT; room temperature; λ_{ex} = 503 nm; λ_{em} = 528 nm. Data are presented as mean ± s.e.m. (standard error of the mean) of three independent experiments.

such as membrane disruption, abnormal cellular signaling, and organelle dysfunction[13,20,24]. The direct interaction between ZF proteins and Aβ, with its consequent impact on Aβ aggregation and toxicity, remains unexplored, however. In this study, we show the complex formation between the

ZF protein PARIS(ZF2–4) and Aβ, with detailed binding properties, as well as the effects of this binding event on Aβ aggregation and cytotoxicity profiles. Furthermore, we demonstrate the sequence-based reactivity and mechanistic details employing a series of PARIS(ZF2–4) fragments and variants. Our findings illuminate a new modulative function of ZF proteins against Aβ amyloidogenesis associated with AD, providing insights into potential therapeutic strategies.

Results and discussion

Binding properties of PARIS(ZF2–4) with Aβ and its reactivity towards Aβ amyloidogenesis.

PARIS(ZF2–4) was recombinantly expressed in *Escherichia coli* (*E. coli*) and subsequently purified[16], as outlined in Supplementary Fig. 1. To determine the binding properties of PARIS(ZF2–4) towards Aβ, we conducted fluorescence-quenching experiments employing fluorophore-conjugated $A\beta_{40}$ ($^{HF488}A\beta_{40}$)[25], as illustrated in Fig. 1c–e. Titration with various concentrations of PARIS(ZF2–4) led to a decrease in the intrinsic fluorescence of $^{HF488}A\beta_{40}$, indicative of their binding (Fig. 1c). In addition, the Job plot obtained by altering the molar ratio between $^{HF488}A\beta_{40}$ and PARIS(ZF2–4) at a fixed total concentration was reached its maximum for a 2:3 PARIS(ZF2–4)-to-$A\beta_{40}$ solution, revealing the PARIS(ZF2–4)-to-$A\beta_{40}$ stoichiometry of *ca*. 1:1.5 (Fig. 1d). Based on the binding stoichiometry, the dissociation constant (K_d) for the PARIS(ZF2–4)–$A\beta_{40}$ adduct was determined to be 0.32 (± 0.01) μM (Fig. 1e). Collectively, our fluorescence quenching analyses reveal that PARIS(ZF2–4) binds to $A\beta_{40}$ with a stoichiometry of approximately 1:1.5, suggesting a specific interaction between the two proteins. Furthermore, the obtained K_d value indicates a sub-micromolar level protein–Aβ interaction[26,27], highlighting the potential role of PARIS(ZF2-4) in altering the aggregation and toxicity profiles of $A\beta_{40}$ (*vide infra*).

To determine the impact of their binding on the aggregation propensity of $A\beta_{40}$, we monitored its aggregation kinetics in the absence and presence of PARIS(ZF2–4) using the turbidity assay, a method for quantifying the amounts of aggregates (Fig. 2a)[25]. As displayed in Fig. 2b, in the absence of PARIS(ZF2–4), $A\beta_{40}$ exhibited characteristic aggregation kinetics, reaching a plateau after *ca*. 5 h of incubation, as evidenced by a sigmoidal curve with a lag phase followed by an elongation stage. Conversely, with equimolar PARIS(ZF2–4), the aggregation kinetics of $A\beta_{40}$ were markedly accelerated exhibiting the decreased lag time (t_{lag}) and half-time ($t_{1/2}$) values (Fig. 2c). The absorbance intensity also surpassed that of PARIS(ZF2–4)-free $A\beta_{40}$ (Fig. 2d and Supplementary Table 1), indicating enhanced and expedited aggregation. In addition, we assessed the aggregation kinetics of $A\beta_{40}$ with sub- and supra-equimolar concentrations of PARIS(ZF2–4) (Fig. 2b–d). The formation of $A\beta_{40}$ aggregates was significantly augmented in a

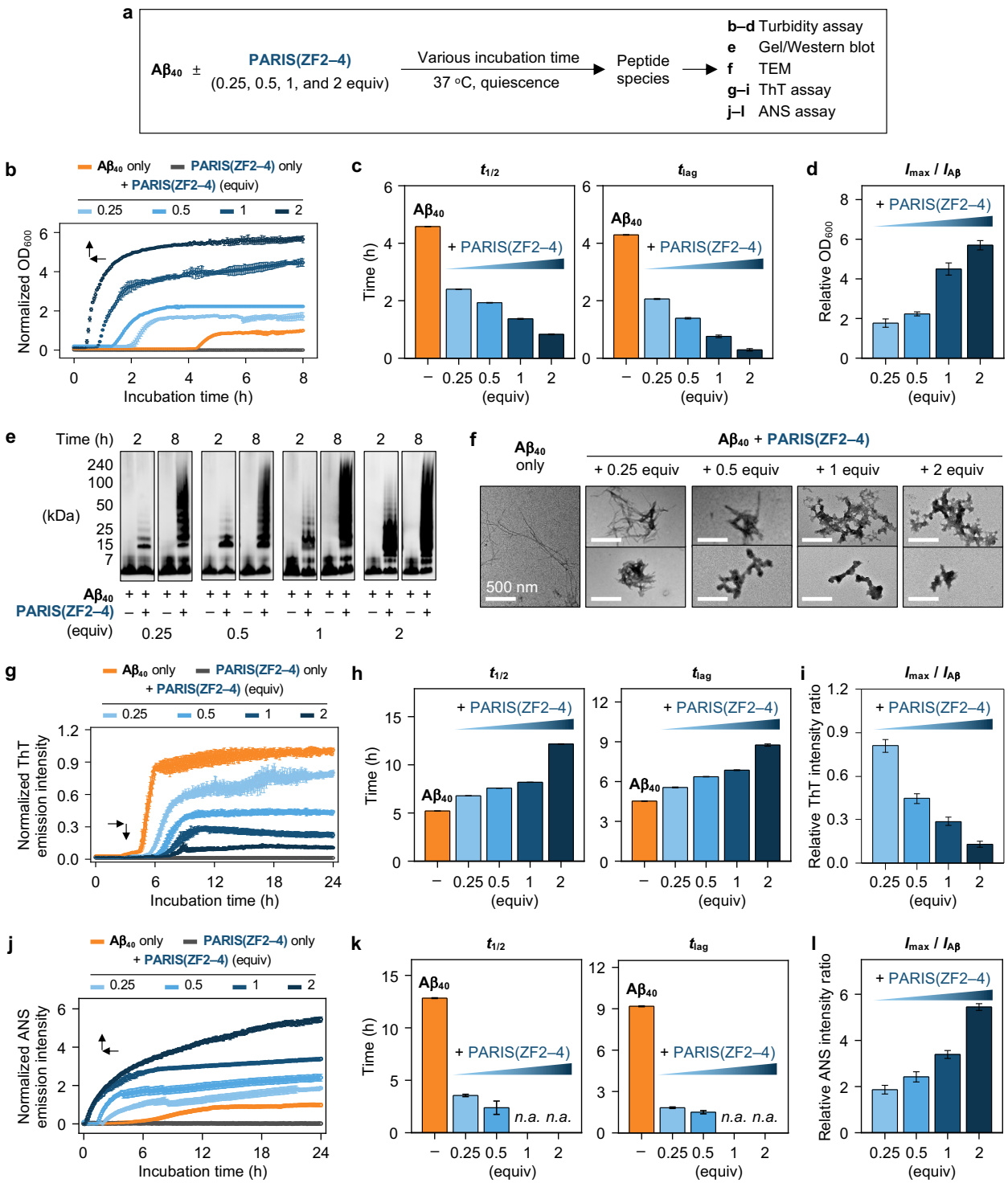

Fig. 2 | Effects of PARIS(ZF2–4) on Aβ40 aggregation. a, Scheme of the aggregation experiments. **b–d,** Aggregation kinetics of Aβ40 upon incubation with and without different concentrations of PARIS(ZF2–4) analyzed by the turbidity assay. The normalized absorbance

intensity was plotted as a function of incubation time and fitted to obtain $t_{1/2}$ and t_{lag} values. Conditions: [Aβ_{40}] = 100 μM; [PARIS(ZF2–4)] = 25, 50, 100, and 200 μM; 20 mM HEPES, pH 7.4, 150 mM NaCl, 1 mM DTT; 37 °C; quiescence; λ_{abs} = 600 nm. Data are presented as mean ± s.e.m. of three independent experiments. **e,** Size distribution of the resultant Aβ_{40} species visualized by tricine–PAGE with Western blotting using an anti-Aβ antibody (6E10). The unprocessed gel images are presented in Supplementary Fig. 3. Conditions: [Aβ_{40}] = 100 μM; [PARIS(ZF2–4)] = 25, 50, 100, and 200 μM; 20 mM HEPES, pH 7.4, 150 mM NaCl, 1 mM DTT; 37 °C; quiescence. **f,** Morphologies of the resultant peptide aggregates generated after 8 h incubation monitored by TEM. Conditions: [Aβ_{40}] = 100 μM; [PARIS(ZF2–4)] = 25, 50, 100, and 200 μM; 20 mM HEPES, pH 7.4, 150 mM NaCl, 1 mM DTT; 37 °C; quiescence. Scale bar = 500 nm. **g–i,** Formation kinetics of β-sheet-rich aggregates in the sample of Aβ_{40} incubated with and without PARIS(ZF2–4) traced by the ThT assay. The normalized emission intensity was plotted as a function of incubation time and fitted to calculate kinetic parameters. **j–l,** Production kinetics of Aβ_{40} aggregates with and without PARIS(Z–4) monitored by the ANS assay. The normalized emission intensity was plotted as a function of incubation time and fitted to calculate kinetic parameters. Conditions: [Aβ_{40}] = 20 μM; [PARIS(ZF2–4)] = 5, 10, 20, and 40 μM; [ThT] = 20 μM; [ANS] = 100 μM; 20 mM HEPES, pH 7.4, 150 mM NaCl, 1 mM DTT; 37 °C; quiescence; (for the ThT assay) λ_{ex} = 440 nm; λ_{em} = 490 nm; (for the ANS assay) λ_{ex} = 350 nm; λ_{em} = 480 nm. *n.a.*, not available. Data are presented as mean ± s.e.m. of three independent experiments.

concentration-dependent manner, suggesting that PARIS(ZF2–4) can promote Aβ_{40} aggregation. Note that PARIS(ZF2–4) itself did not assemble under our experimental conditions.

Next, we examined the molecular weight distribution of Aβ_{40} (4–240 kDa) following incubation with and without PARIS(ZF2–4) using gel electrophoresis and Western blotting with an anti-Aβ antibody (6E10). As depicted in Fig. 2e, distinct from the samples of PARIS(ZF2–4)-free Aβ_{40}, upon treatment with 0.25 equiv of PARIS(ZF2–4) for 8 h, a band at *ca*. 15 kDa with smearing ranging from 15 to 240 kDa appeared, indicative of forming diverse Aβ_{40} aggregates. This trend persisted under conditions of higher PARIS(ZF2–4) concentrations. A new band at *ca*. 15 kDa, potentially assigned to be a 1:1 PARIS(ZF2–4)-to-Aβ_{40} complex, was further confirmed by additional tricine–PAGE using purified fluorophore-labeled PARIS(ZF2–4), ^{HF555}PARIS(ZF2–4). As displayed in Supplementary Fig. 2, a band at *ca*. 15 kDa was detected in both tricine–PAGE

with ^{HF555}PARIS(ZF2–4) and 6E10 with a gradual decrease in intensity of a peak at *ca*. 10 kDa corresponding to PARIS(ZF2–4). This suggests the complex formation between PARIS(ZF2–4) and Aβ_{40}. The morphology of the resultant large-sized aggregates (> 240 kDa) was visualized by transmission electron microscopy (TEM) (Fig. 2f). The morphology of Aβ_{40} aggregates produced with sub-equimolar concentrations of PARIS(ZF2–4) appeared as a mixture of fibrils and amorphous aggregates, whereas the sample of Aβ_{40} alone displayed linear fibrils. With higher amounts of PARIS(ZF2–4), more large-sized amorphous structures were observed without fibrils even after 8 h of incubation.

To further probe the production of amorphous structures upon aggregation of Aβ_{40} with PARIS(ZF2–4), we investigated the change in the secondary structures of Aβ_{40} incubated with and without PARIS(ZF2–4) by circular dichroism (CD) spectroscopy (Supplementary Fig. 4). We selected an Aβ_{40}-to-PARIS(ZF2–4) ratio of 1:0.25 to minimize the signals from PARIS(ZF2–4). The CD spectra obtained from the sample of Aβ_{40} without PARIS(ZF2–4) showed a conformational transition from random coil to β-strand within 4 h of incubation, as evidenced by a shift in the local minimum from *ca*. 202 nm to *ca*. 225 nm. Interestingly, under PARIS(ZF2–4)-present conditions, the random coil conformation in Aβ_{40} was maintained even after 6 h of incubation, suggesting its delayed conformational change into fibrils by PARIS(ZF2–4).

The extent of β-sheet-rich Aβ_{40} aggregates was kinetically quantified upon aggregation with and without PARIS(ZF2–4) by the thioflavin-T (ThT) assay, a method for quantifying the formation of β-sheet-rich aggregates[25,28,29] (Fig. 2g). A nucleation-dependent fibrillar aggregation process was observed without PARIS(ZF2–4), characterized by a sigmoidal curve with lag, elongation, and plateau phases with the t_{lag} and $t_{1/2}$ values of 4.53 (± 0.02) h and 5.21 (± 0.01) h, respectively. In contrast, incubation of Aβ_{40} with PARIS(ZF2–4) resulted in prolonged kinetic parameters as a function of the concentration of PARIS(ZF2–4) (Fig. 2h). Additionally, the maximum ThT emission intensity, reflecting the amount of ThT-reactive structures reached at the plateau, was prominently decreased in a concentration-dependent manner with PARIS(ZF2–4) (Fig. 2i).

We also performed the 8-anilino-1-naphthalenesulfonate (ANS) assay of which fluorescence increases in a hydrophobic environment, useful to monitor the amorphous aggregation and fibrilization[30] (Fig. 2j). Given that amorphous aggregates contain more hydrophobic surface exposed to solvents, relative to fibrils, an increase in ANS fluorescence with and without the lag stage represent the formation of fibrils and amorphous structures, respectively[30]. As expected, a sigmoidal curve with the t_{lag} and $t_{1/2}$ values of 9.20 (± 0.03) h and 12.83 (± 0.03) h, respectively, was observed when Aβ_{40} was incubated without PARIS(ZF2–4),

while the relatively faster aggregation kinetics, indicative of forming amorphous aggregates, were observed upon $A\beta_{40}$ aggregation with PARIS(ZF2–4) (Fig. 2k). The maximum emission intensity of ANS was also enhanced in a dose-dependent manner of PARIS(ZF2–4) (Fig. 2l). These collective results indicate that PARIS(ZF2–4) redirects the on-pathway toxic amyloidogenesis of $A\beta_{40}$ into amorphous aggregation.

Moreover, we investigated whether PARIS(ZF2–4) can alter the aggregation propensity of $A\beta_{42}$, another major isoform of Aβ showing distinct aggregation dynamics[13,20,31]. As presented in Supplementary Fig. 5a–c, the incubation of $A\beta_{42}$ with sub-equimolar concentrations of PARIS(ZF2–4) resulted in its delayed and reduced fibrillization, relative to $A\beta_{42}$ alone, as observed by the ThT assay. The morphologies of the resultant aggregates, visualized by TEM, indicated a mixture of fibrils and less structured aggregate, or amorphous aggregates without fibrils (Supplementary Fig. 5d). Notably, higher amounts of PARIS(ZF2–4) did not increase the ThT emission intensity even after 24 h of incubation, leading to the production of larger amorphous structures. This highlights the ability of PARIS(ZF2–4) to noticeably modify the aggregation of $A\beta_{42}$, in addition to $A\beta_{40}$. Taken together, PARIS(ZF2–4) alters Aβ aggregation behaviors, promoting the amorphous aggregation of Aβ to different extents depending on the PARIS(ZF2–4)-to-Aβ stoichiometry, as expected from the binding properties of PARIS(ZF2–4) with Aβ (*vide supra*). The conversion of Aβ peptides into amorphous aggregates has been reported to be less toxic[32-34] and, thus, Aβ-associated cytotoxicity is possibly mitigated by PARIS(ZF2–4) (*vide supra*).

Impact of PARIS(ZF2–4) on $A\beta_{40}$-induced cytotoxicity. Given that PARIS(ZF2–4) accelerates the amorphous aggregation of $A\beta_{40}$, supposed to be less toxic, we evaluated whether this redirection alters $A\beta_{40}$-triggered cytotoxicity by conducting two types of experiments: (method I) extracellular and (method II) intracellular conditions (Fig. 3a). In an extracellular system, the interaction of Aβ with cell membranes can induce cytotoxicity *via* various mechanisms, including receptor blockade and ion channel formation[21,35]. Thus, the samples obtained by pre-incubation with different PARIS(ZF2–4)-to-$A\beta_{40}$ ratios for 8 h were applied to human neuroblastoma SH-SY5Y cells for 48 h, and their cell survival and interaction with cell membranes were analyzed by the MTT assay [MTT = 3-(4,5-dimethylthiaol-2-yl)-2,5-diphenyltetrazolium bromide] and immunocytochemistry (ICC) studies, respectively. As expected, the cytotoxicity observed by $A\beta_{40}$ alone was significantly mitigated by *ca*. 10–20% in the presence of PARIS(ZF2–4), as the concentration of PARIS(ZF2–4) increased (Fig. 3b). Note that PARIS(ZF2–4) itself did not exhibit noticeable cytotoxicity under our experimental conditions.

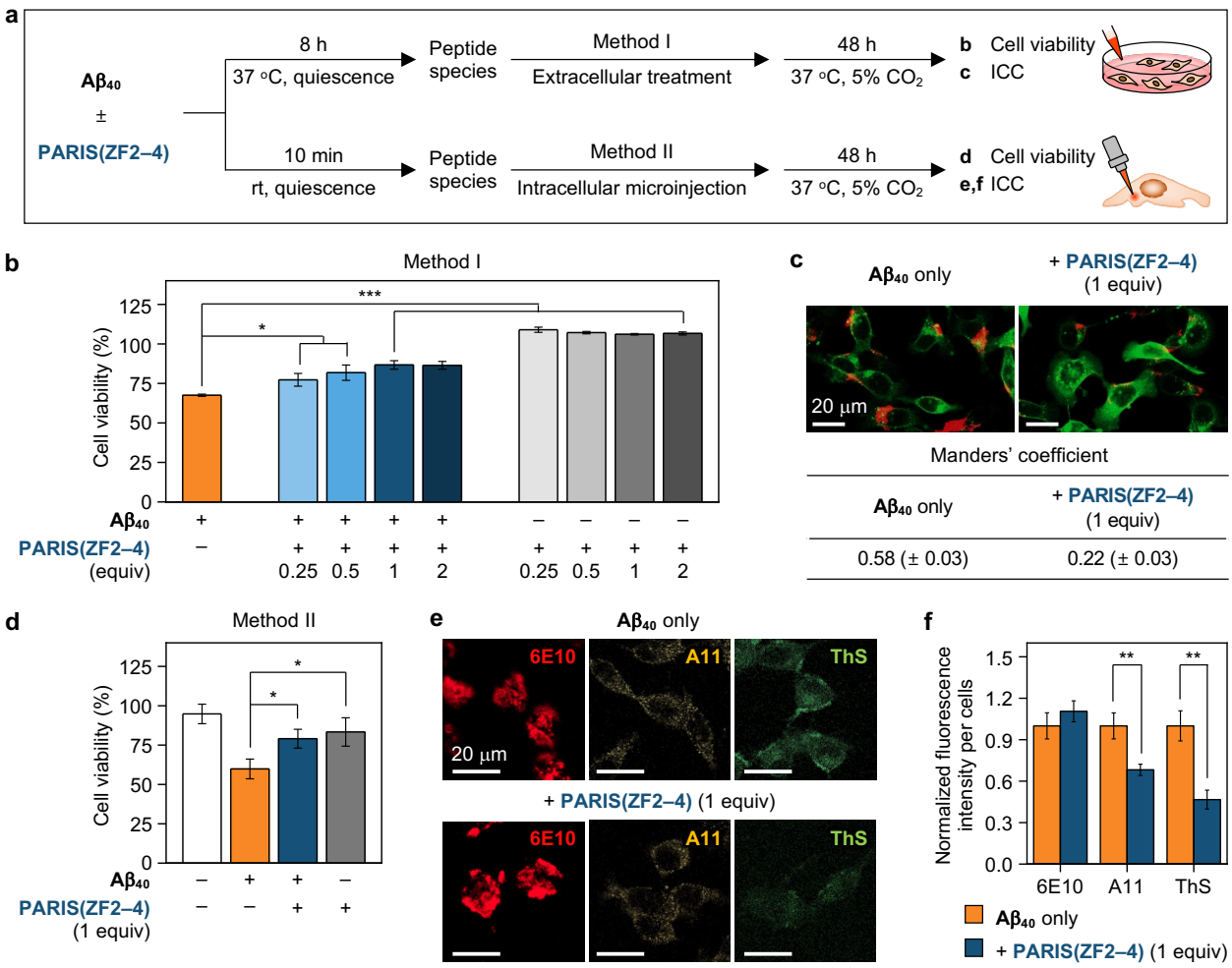

Fig. 3 | Influence of PARIS(ZF2–4) on the cytotoxicity induced by $A\beta_{40}$. a, Scheme of the live-cell studies. **b,** Survival of the cells extracellulary treated with either $A\beta_{40}$, PARIS(ZF2–4), or both determined by the MTT assay. Cell viability was calculated in comparison to that with an equivalent amount of the buffered solution. Conditions: [$A\beta_{40}$] = 10 μM; [PARIS(ZF2–4)] = 2.5, 5, 10, and 20 μM; 20 mM HEPES, pH 7.4, 150 mM NaCl; 37 °C; quiescence; SH-SY5Y cells that were non-differentiated; incubation with cells for 48 h. *P < 0.1, ***P < 0.001; n = 3; Student's t-test. Data are presented as mean ± s.e.m. **c,** Live-cell localization of $A\beta_{40}$ that was extracellularly added and incubated in the absence and presence of PARIS(ZF2–4) measured by ICC studies. Conditions: [$A\beta_{40}$] = 10 μM; [PARIS(ZF2–4)] = 10 μM; 20 mM HEPES, pH 7.4, 150 mM NaCl; 37 °C; quiescence; SH-SY5Y cells that were non-differentiated; incubation with cells for 48 h. Scale bar = 20 μm. Data are presented as mean ± s.e.m. of three independent experiments. **d,** Viability of the cells microinjected with either $A\beta_{40}$, PARIS(ZF2–4), or both. Cell survival measurements were described in details in the experimental section. Conditions: [$A\beta_{40}$] = 10 μM;

[PARIS(ZF2–4)] = 10 μM; [Texas Red-labeled dextran] = 0.5 mg/mL; 20 mM HEPES, pH 7.4, 150 mM NaCl; SH-SY5Y cells that were non-differentiated; incubation with cells for 48 h. *P < 0.1; n = 3–5; Student's t-test. Data are presented as mean ± s.e.m. **e,f,** Fluorescence images of the cells intracellularly injected with $A\beta_{40}$ added with and without PARIS(ZF2–4). $A\beta_{40}$ species were visualized by immunostaining [primary antibodies, 6E10 (anti-Aβ antibody; red) and A11 (anti-oligomer antibody; orange) with fluorescent-conjugated secondary antibodies] or fluorescent dyes [ThS for Aβ fibrils (green)] and emission intensities were quantified. Images were taken by confocal microscopy in nine or more randomly selected fields per condition. Conditions: [$A\beta_{40}$] = 10 μM; [PARIS(ZF2–4)] = 10 μM; 20 mM HEPES, pH 7.4, 150 mM NaCl; SH-SY5Y cells that were non-differentiated; incubation with cells for 48 h. Scale bar = 20 μm. **P < 0.01; n = 34–58; Student's t-test. Data are presented as mean ± s.e.m.

The ICC studies in SH-SY5Y cells supported the decrease in the cytotoxicity of $A\beta_{40}$ by visualizing the interaction of $A\beta_{40}$ species with cell membranes in the absence and presence of PARIS(ZF2–4) (Fig. 3c). Cells were treated with $A\beta_{40}$ species produced with and without PARIS(ZF2–4), followed by staining cellular membranes and Aβ using a fluorescent membrane dye and a fluorophore-conjugated antibody, respectively. The co-localization quantity of interest was quantified by the Manders coefficient, which indicates the fraction of one probe coincident with the second probe[35]. Notably, the coefficient value of PARIS(ZF2–4)-treated $A\beta_{40}$ species was diminished by *ca*. 60%, compared to that of PARIS(ZF2–4)-free $A\beta_{40}$ species [0.58 (± 0.03)]. These observations confirm the decreased interaction between cell membranes and $A\beta_{40}$ species generated with PARIS(ZF2–4), which is anticipated from the aggregation studies.

Moving forward, we performed microinjection experiments to determine the influence of PARIS(ZF2–4) on the cytotoxicity associated with intracellular $A\beta_{40}$ (Fig. 3d). Solutions containing either $A\beta_{40}$, PARIS(ZF2–4), or both were mixed with Texas Red-labeled dextran, an indicator for the cells, and then injected into live cells. The samples were not pre-incubated to prevent the formation of large aggregates that could clog the microinjection capillary. After 48 h of incubation, cell viability was assessed by counting Texas Red-positive cells using previously reported methods[36]. The injection of $A\beta_{40}$ treated with PARIS(ZF2–4) inside the cells resulted in approximately a 20% increase in cell survival compared to that of $A\beta_{40}$ alone. Note that PARIS(ZF2–4) itself did not induce significant cell death under our experimental conditions. Additionally, to verify whether the presence of PARIS(ZF2–4) affects the aggregation of $A\beta_{40}$ in

an intracellular system, we carried out the aggregate analysis by immunostaining with an anti-oligomer antibody (A11) and thioflavin-S (ThS), which can detect Aβ oligomers and fibrils, respectively[25,37] (Fig. 3e). As anticipated from our aggregation studies (*vide supra*), the amounts of oligomeric and fibrillar aggregates were significantly reduced by *ca*. 30% and 55%, respectively, when cells were injected with $A\beta_{40}$ treated with PARIS(ZF2–4) (Fig. 3f). Given that A11-positive oligomers, as well as protofibrils and fibrils detectable by ThS, are reported to be toxic[21,22,37,38], these findings support the role of PARIS(ZF2–4) in promoting the formation of less toxic amorphous $A\beta_{40}$ aggregates within intracellular environments. Collectively, our cell studies manifest that PARIS(ZF2–4) can reduce Aβ's interaction with cell membranes and prevent the formation of intracellular oligomers and fibrils, thus alleviating Aβ-associated cytotoxicity.

Direct interaction of PARIS(ZF2–4) with $A\beta_{40}$ and potential binding modes. To provide mechanistic insights into how PARIS(ZF2–4) facilitates less toxic amorphous aggregation of $A\beta_{40}$, we investigated the detailed direct binding properties of PARIS(ZF2–4) to monomeric $A\beta_{40}$ in solution using ^{15}N-labeled $A\beta_{40}$ and 2D ^{1}H–^{15}N SOFAST–HMQC NMR spectroscopy (Fig. 4a). As depicted in Fig. 4b,c, a decrease in the peak intensity across all amino acid residues of $A\beta_{40}$ by *ca*. 40% presented the formation of NMR-invisible aggregates with treatment of PARIS(ZF2–4), highlighting PARIS(ZF2–4)'s binding with Aβ and effect on Aβ aggregation dynamics. Concurrently, some chemical shift perturbations (CSPs) at specific residues, including Asp7, Ser26, and Val36 of ^{15}N-labeled $A\beta_{40}$, were observed upon exposure to a supra-equivalent concentration of PARIS(ZF2–4). Notably, Val36, a residue involved in a hydrophobic interaction with the self-recognition site that is a major driving force of Aβ aggregation, in addition to its involvement in β-turn motifs within fibrillary architectures[13,39], exhibited a CSP, suggesting alterations in the conformational dynamics and aggregation propensity of $A\beta_{40}$ (Fig. 4c). Furthermore, the amino acid residues of PARIS(ZF2–4) were monitored by addition of $A\beta_{40}$ using ^{15}N-labeled PARIS(ZF2–4) obtained from *E. coli*. and 2D ^{1}H–^{15}N HSQC NMR spectroscopy (Supplementary Fig. 6). NMR spectra displayed the reduced peak intensity by *ca*. 20%, with some CSPs at multiple residues of PARIS(ZF2–4), when $A\beta_{40}$ was applied. These observations corroborate the direct binding between the two proteins, indicating the amino acid residues of $A\beta_{40}$ affected by PARIS(ZF2–4).

Moving forward, to elucidate the atomistic details of putative PARIS(ZF2–4)–$A\beta_{40}$ binding modes, we modeled the heterodimeric interface between these two proteins, favoring scenarios

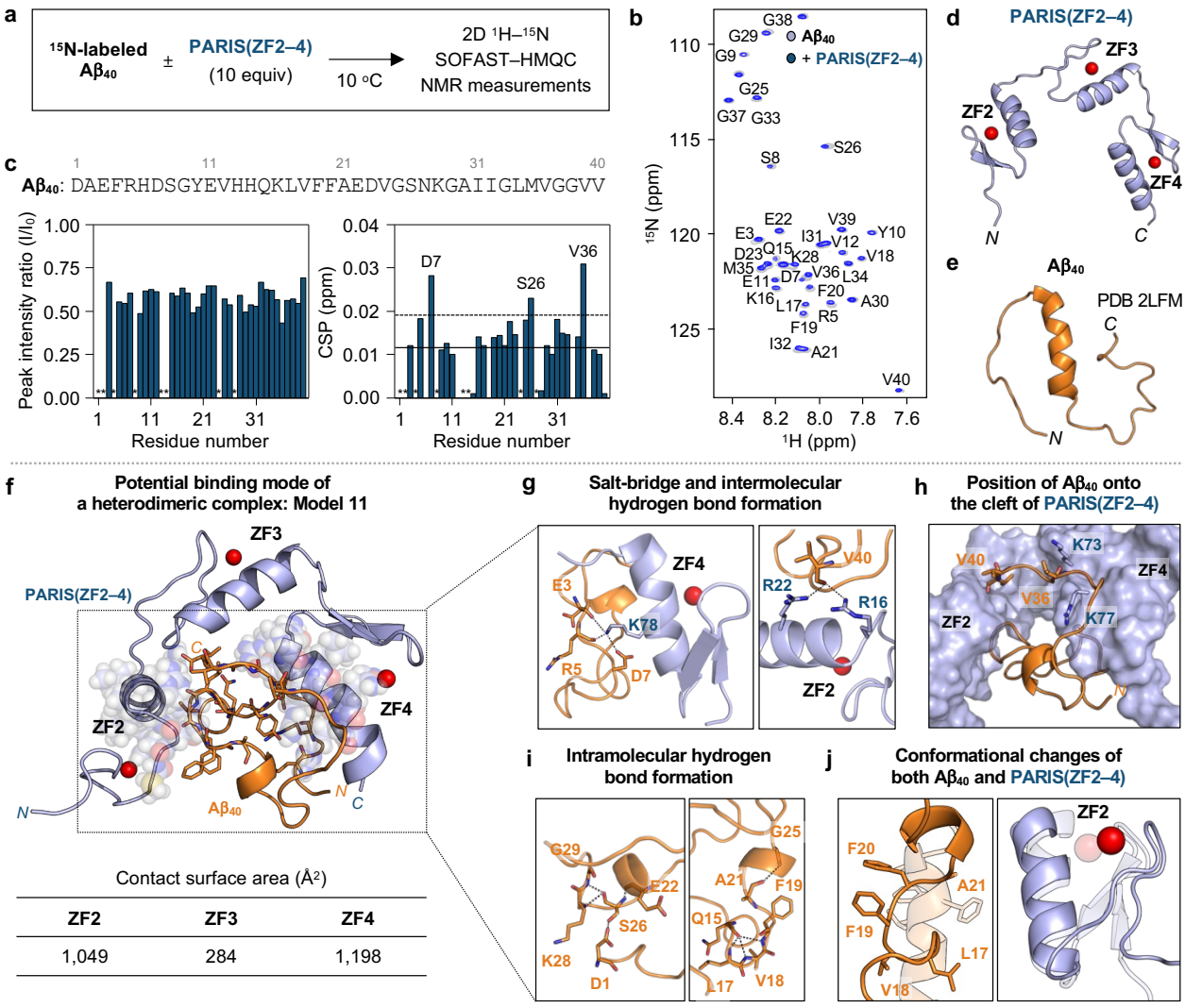

Fig. 4 | Interaction of Aβ$_{40}$ with PARIS(ZF2–4). a, Scheme of 2D ^{1}H–^{15}N SOFAST–HMQC NMR (800 MHz) experiments. **b,c,** NMR analyses of ^{15}N-labeled Aβ$_{40}$ upon addition of PARIS(ZF2–4). The average of CSPs and average + one standard deviation are indicated with solid and dashed lines, respectively. Conditions: [^{15}N-labeled Aβ$_{40}$] = 20 μM; [PARIS(ZF2–4)] = 200 μM; 20 mM HEPES, pH 7.4, 1 mM DTT, 10% v/v D_2O; 10 °C. The unresolved peaks are noted with asterisks. **d,e,** Conformations of PARIS(ZF2–4) predicted by AlphaFold2[41,42], followed by docking three zinc ions, and Aβ$_{40}$ (PDB 2LFM[43]) used for MD simulations. Note that AlphaFold2 modeled the structures of ZF proteins based on the database (their Zn(II)-bound forms). **f,** A representative model of the PARIS(ZF2–4)–Aβ$_{40}$ heterodimer obtained from the trajectories of MD simulations over 2.5 μs. PARIS(ZF2–4) and Aβ$_{40}$ are depicted in skyblue and orange, respectively. **g–j**, Detailed analysis of Model 11. Possible hydrogen bonds within 3.0 Å are indicated with dashed

black lines. The cleft generated by PARIS(ZF2–4) is shown in the space-filling representation. Each monomeric model of $A\beta_{40}$ and PARIS(ZF2–4) was superimposed with transparency. MD simulations focusing on the conformational changes within the ZF2 region of PARIS(ZF2–4) upon binding to $A\beta_{40}$ are presented in Supplementary Video 1.

of negative cooperativity[40] over those involving the 1:2 PARIS(ZF2–4)-to-$A\beta_{40}$ adduct. As the experimentally determined structures of PARIS(ZF2–4) were unavailable, we employed AlphaFold2[41,42] to generate an initial structural model of PARIS(ZF2–4) (Fig. 4d). In the case of monomeric $A\beta_{40}$, we used a structure (PDB 2LFM[43]) derived from solution NMR experiments (Fig. 4e). Acknowledging the intrinsically disordered nature of $A\beta_{40}$[13], we aimed to refine its structure *via* protein docking and subsequent molecular dynamics (MD) simulations. Through protein–protein docking simulations[44], we produced twelve candidate models of the heterodimeric interface between PARIS(ZF2–4) and $A\beta_{40}$ (Supplementary Fig. 7). These models were further evaluated for their relative stabilities using MD simulations[36,45,46], as summarized in Supplementary Figs. 8 and 9. Notably, one particular model (Model 11 depicted in Fig. 4f) among twelve models exhibited persistent maintenance of the dimeric interface throughout microsecond-level MD simulations lasting up to 2.5 μs supposed to be a relatively stable protein–protein interaction[47]. Thus, this model was further analyzed to suggest a plausible binding mode for the PARIS(ZF2–4)–$A\beta_{40}$ complex, offering valuable insights into their interaction dynamics at the atomic level.

In Model 11, the heterodimeric interface spanned a contact surface area (CSA) of 2,315 $Å^2$, calculated based on the difference in the solvent-accessible surface area of individual monomers and the heterodimer, which was averaged over the MD trajectories from 0.5 μs to 2.5 μs. This CSA corresponded to a favorable binding energy of 17 kcal/mol, when considering the unit area contributes 7.2 cal/mol/$Å^2$ of favorable interaction[48]. Detailed analysis further revealed that the CSA between the ZF2 and ZF4 domains from PARIS(ZF2–4) and $A\beta_{40}$ was 1,049 $Å^2$ and 1,198 $Å^2$, respectively, while that involving the ZF3 domain and $A\beta_{40}$ measured 284 $Å^2$ (Fig. 4f). These observations confirm that the intermolecular contacts between PARIS(ZF2–4) and $A\beta_{40}$ are predominantly mediated by the ZF2 and ZF4 domains, indicating them as the critical motifs for binding with $A\beta_{40}$ and, subsequently, ensuing the modulative function of PARIS(ZF2–4) against $A\beta_{40}$ amyloidogenesis.

The presence of stable heterodimeric interface prompted us to quantify the binding energy

of the heterodimer. We applied the molecular mechanics/poisson-Boltzmann surface area method, which incorporates the Coulombic ($\Delta E_{Coulomb}$) and the van der Waals (ΔE_{vdW}) energies in gas phase and the polar (ΔG_{PB}) and the non-polar (ΔG_{NP}) solvation energies in aqueous environment[46]. The computed binding energy (ΔG_{bind}) was –11.4 kcal/mol when averaged over the last 2.0 μs MD trajectories. The computed binding energy was in good agreement with our experimentally determined K_d value for the PARIS(ZF2–4)–Aβ_{40} adduct [K_d = 0.32 (± 0.01) μM; Fig. 1e], which corresponds to –8.8 kcal/mol of binding energy. The gross sum of $\Delta E_{Coulomb}$, ΔE_{vdW}, ΔG_{PB}, and ΔG_{NP} was –40.7 kcal/mol, suggesting the presence of favorable attractive interactions across the dimeric interface. Note that the attractive interaction can overcome the energy cost to overcome the translational and rotational entropies upon formation of the dimer [$-T(\Delta S_{trans} + \Delta S_{rot})$ = 29.4 kcal/mol].

The stability of the heterodimeric interface observed in MD simulations was supported by detailed intermolecular interactions. As illustrated in Fig. 4g, the CSP at the Asp7 residue of Aβ_{40} indicated its involvement in an ionic contact (salt bridge) with the Lys78 residue of PARIS(ZF2–4), which neutralizes the electrostatic charge in the *N*-terminal region of Aβ_{40}, thereby mitigating electrostatic repulsion that could interfere with Aβ aggregation[36,49]. Moreover, intermolecular hydrogen bonds involving Lys78 of PARIS(ZF2–4) with Glu3 and Arg5 located at the *N*-terminal region of Aβ_{40} were identified. The hydrophobic *C*-terminal residues of Aβ_{40}, particularly Val36–Val40, positioned within the cleft generated by PARIS(ZF2–4), potentially engaging in extensive hydrophobic and polar contacts with neighboring amino acids of PARIS(ZF2–4) (Fig. 4h). Specifically, the Val36 residue situated within the cleft between Lys73 and Arg77 within the ZF4 domain of PARIS(ZF2–4) experienced a prominent chemical shift due to transfer to a dehydrated microscopic environment. Additionally, the *C*-terminal carboxyl group of Aβ_{40} formed hydrogen bonds with the side chains of Arg16 and Arg22 within the ZF2 segment of PARIS(ZF2–4) (Fig. 4g). These interactions collectively contribute to the stability of the heterodimeric interface and, subsequently, modify the aggregation properties of Aβ (*vide supra*).

In addition to intermolecular contacts between the two proteins, intramolecular hydrogen bonding networks within Aβ_{40} upon binding to PARIS(ZF2–4) were detected (Fig. 4i). The hydroxyl moiety from Ser26 formed side chain–side chain hydrogen bond with Asp1. Moreover, the backbone carbonyl and amino groups of Ser26 engaged in hydrogen bonding with the backbone amide moiety of Glu22, Lys28, and Gly29. Lastly, additional intramolecular hydrogen bonds within the self-recognition site (Leu17–Ala21) of Aβ_{40}, specifically Gln15 with Leu17, Val18, and Phe19 as well as Ala21 with Gly25, were found. These intramolecular interactions can further stabilize

the PARIS(ZF2–4)–Aβ_{40} complex.

Our MD simulations revealed conformational changes in both PARIS(ZF2–4) and Aβ_{40} (Fig. 4j). PARIS(ZF2–4) maintained its ZF motifs bound to Zn(II), consistent with the monomeric model, while a β-hairpin motif originally observed in the regions spanning Leu5–Cys7 and Gly11–Phe14 within the ZF2 domain disappeared upon binding to Aβ_{40}, however (Supplementary Video 1 and Fig. 4d,j). This loss, with the pronounced intermolecular contacts between ZF2 and Aβ_{40}, may play a pivotal role in the reactivity of PARIS(ZF2–4) towards Aβ_{40} amyloidogenesis. In the case of Aβ_{40}, its secondary structure spanning from His13 to Ala21, including the self-recognition site essential for its aggregation[13,20], became substantially disordered, diverging from its intrinsic α-helical structure (Fig. 4e,j). This suggests that PARIS(ZF2–4) alters the propensity of Aβ aggregation. Our experimental and computational results validate that the ZF2 and ZF4 regions from PARIS(ZF2–4) primarily bind to the *N*- and *C*-terminal regions of Aβ_{40} and induce the conformational changes, leading to the alteration in Aβ's aggregation patterns. This highlights a potential role of the β-hairpin structures in PARIS(ZF2–4).

Sequence-based reactivity and mechanistic studies towards Aβ_{40} aggregation and cytotoxicity. Given that our detailed binding studies highlight specific ZF motifs with a β-hairpin structure responsible for altering the aggregation of Aβ, we conducted comprehensive sequence–reactivity relationship studies employing PARIS(ZF2–4) fragments and ZF2' variants to elucidate these implications in detail. We first prepared PARIS(ZF2–4) fragments (ZFx'; Fig. 5a), namely ZF2', ZF3', and ZF4', each harboring a distinct ZF segment from PARIS(ZF2–4), and probed their reactivity with Aβ_{40}. As shown in the turbidity assay results (Fig. 5b), distinct from PARIS(ZF2–4), ZF2' and ZF4' induced a biphasic growth pattern in Aβ_{40} aggregation, while ZF3' displayed negligible reactivity. The absorbance intensity of Aβ_{40}, influenced by equimolar ZF2' and ZF4', was *ca*. 2.8- and 1.7-fold higher, respectively, than that of Aβ_{40} alone, with accelerated aggregation kinetics (Fig. 5c and Supplementary Table 1). The concentrations of ZF2' or ZF4' were correlated with enhanced aggregation dynamics, reflected in increased maximum absorbance intensity and faster kinetics. Morphological analysis revealed that Aβ_{40} aggregates formed with sub-equimolar concentrations of ZF2' and ZF4' appeared as a mixture of chopped fibrils and less structured aggregates (Fig. 5d and Supplementary Fig. 10), reported to be less toxic[32-34]. When the concentrations of ZF2' and ZF4' were increased, amorphous aggregates without fibrils were generated even after 8 h of incubation, whereas incubation with ZF3' did not

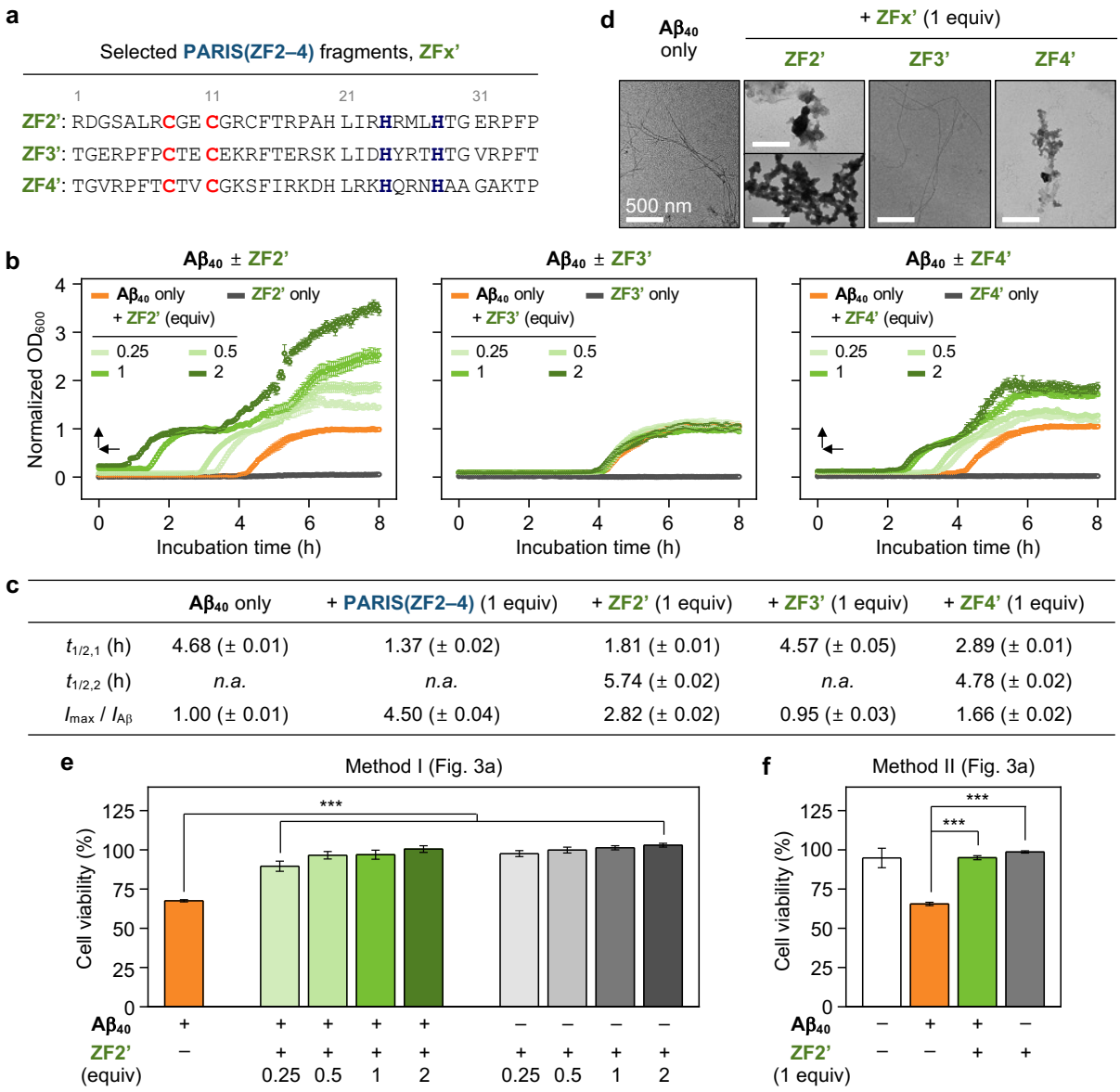

Fig. 5 | Effects of PARIS(ZF2–4) fragments towards Aβ$_{40}$ aggregation and cytotoxicity. a, Domain organization of PARIS(ZF2–4) and its selected fragments containing one ZF segment, (either ZF2', ZF3', or ZF4'). The cystein and histidine residues involved in Zn(II) coordination are highlighted in bold red and navy, respectively. **b,c,** Aggregation kinetics of Aβ$_{40}$ upon incubation with and without different concentrations of PARIS(ZF2–4) fragments [ZFx'; Zn(II)-bound form] analyzed by the turbidity assay. The kinetic parameters of Aβ$_{40}$ incubated with and without PARIS(ZF2–4) or ZFx' were obtained by fitting the absorbance curves using the modified Boltzmann-sigmoidal or double Boltzmann-sigmoidal equations. *n.a.* not available. Note that the $t_{1/2,2}$ value of Aβ$_{40}$ aggregation showing a monophasic growth is not defined. Conditions: [Aβ$_{40}$] =

100 μM; [apo-ZFx'] = 25, 50, 100, and 200 μM; [Zn(II)] = 22.5, 45, 90, and 180 μM; 20 mM HEPES, pH 7.4, 150 mM NaCl, 1 mM DTT; 37 °C; quiescence; λ_{abs} = 600 nm. Note that 0.9 equiv of Zn(II) was added to apo-ZFx' and incubated for 3 min to avoid the presence of free Zn(II). Data are presented as mean ± s.e.m. of three independent experiments. **d,** Morphologies of the resultant $A\beta_{40}$ aggregates incubated with and without ZFx' visualized by TEM. Conditions: [$A\beta_{40}$] = 100 μM; [apo-ZFx'] = 100 μM; [Zn(II)] = 90 μM; 20 mM HEPES, pH 7.4, 150 mM NaCl, 1 mM DTT; 37 °C; quiescence. Scale bar = 500 nm. **e,** Viability of the cells treated with either $A\beta_{40}$, ZF2', or both determined by the MTT assay. Cell survival was calculated in comparison to that with an equivalent amount of the buffered solution. Influence of ZF3' and ZF4' on the cytotoxicity of $A\beta_{40}$ was depicted in Supplementary Fig. 12. Conditions: [$A\beta_{40}$] = 10 μM; [apo-ZF2'] = 2.5, 5, 10, and 20 μM; [Zn(II)] = 2.25, 4.5, 9, and 18 μM; 20 mM HEPES, pH 7.4, 150 mM NaCl; 8 h pre- and 48 h post-incubation; 37 °C; quiescence; SH-SY5Y cells that were non-differentiated. ***P < 0.001; n = 3; Student's *t*-test. Data are presented as mean ± s.e.m. **f,** Viability of the cells microinjected either $A\beta_{40}$, ZF2', or both. Cell survival measurements were described in details in the experimental section. Conditions: [$A\beta_{40}$] = 10 μM; [apo-ZF2'] = 10 μM; [Zn(II)] = 9 μM; [Texas Red-labeled dextran] = 0.5 mg/mL; 20 mM HEPES, pH 7.4, 150 mM NaCl; SH-SY5Y cells that were non-differentiated; incubation with cells for 48 h. ***P < 0.001; n = 3; Student's *t*-test. Data are presented as mean ± s.e.m.

affect the morphology of $A\beta_{40}$ aggregates. Aligning with these observations, equimolar ZF2' and ZF4' led to an increase in ANS fluorescence without the lag phase, indicative of forming amorphous aggregates (Supplementary Fig. 11).

As expected, treatments with ZF2' and ZF4' enhanced cell viability against the cytotoxicity induced by $A\beta_{40}$ alone by *ca*. 20–30% and 10–20%, respectively, in a concentration-dependent manner [for PARIS(ZF2–4), 10–20%], while ZF3' did not mitigate the cytotoxicity associated with $A\beta_{40}$ (Fig. 5e and Supplementary Fig. 12). These investigations highlight that PARIS(ZF2–4)'s reactivity with $A\beta_{40}$ is primarily involved in the contributions of either ZF2', ZF4', or both. Importantly, ZF2' indicated a greater ability to rescue $A\beta_{40}$-triggered cytotoxicity compared to ZF4' and even PARIS(ZF2–4). Intracellular studies revealed that the co-administration of ZF2' and $A\beta_{40}$ led to a 30% increase in cell survival, relative to $A\beta_{40}$ alone, as well as a 70% reduction in ThS fluorescence, supporting its ability to produce less toxic Aβ aggregates (Fig. 5f and Supplementary Fig. 13).

Following our aggregation and cell studies on ZFx', we questioned why ZF2' and ZF4' over ZF3' facilitate the amorphous aggregation of $A\beta_{40}$ to different extents. We turned to the AlphaFold2-predicted structure of PARIS(ZF2–4), as depicted in Fig. 4d, to investigate their structural differences. The PARIS(ZF2–4) structure revealed the presence of random coils, α-helices, and two β-hairpin motifs within the ZF2 and ZF4 domains. Conversely, the ZF3 domain lacked a β-strand moiety, prompting further exploration of the structural distinctions of ZFx'. As shown in the CD measurements (Fig. 6a,b), distinct from ZF2' and ZF4', ZF3' exhibited a relatively low intensity at the local minimum of *ca*. 225 nm, showing a decrease in the β-strand population [for ZF2', 32.9 (± 4.4)%; for ZF3', 7.8 (± 5.1)%; for ZF4', 19.8 (± 4.2)%]. Consistent with our spectroscopic analysis, AlphaFold2[41,42]-predicted ZF2' and ZF4' exhibited two anti-parallel β-strands linked by a short loop, while ZF3' lacked a β-hairpin motif (Fig. 6c), corroborating the significance of specific ZF motifs with a β-hairpin structure dictating PARIS(ZF2–4)'s modulative function against Aβ amyloidogenesis.

To delineate the importance of the β-strand motifs in controlling the reactivity of ZF2' against $A\beta_{40}$ amyloidogenesis, we strategically designed two series of ZF2' variants (Mx, 44 variants in total; Supplementary Fig. 14), engineered to either include or exclude the β-hairpin within their structures by altering amino acid residues in the β_1 or β_2 region based on the ZF2' framework. Our structural screening using AlphaFold2 predictions[41,42] suggested that Mx consistently contains a β-hairpin when the amino acid sequence of the β_2 portion begins with a Gly residue, regardless of the components in β_1. In contrast, Mx containing the Glu12 residue did not show the β-strand moiety, except for M32, M38, and M41, which share the common sequence Phe6-Tyr7-Cys8. As illustrated in Fig. 6d–f and Supplementary Fig. 14, among multiple ZF2' variants, those with a relatively abundant β-strand character, such as M28 and M32, were selected to evaluate the reactivity of Mx towards $A\beta_{40}$, compared to their parent forms, M13 and M30, with the absence of β-strand conformation. As presented in Fig. 6g–j and Supplementary Figs. 15–17, the β-hairpin-containing M28 and M32 were confirmed to enhance the amorphous aggregation of $A\beta_{40}$, resulting in less toxic amorphous aggregates; however, this reactivity was not observed with M13 and M30 without β-strand, even within the ZF2' framework. Notably, M28, M32, and ZF2', which share the ZF2' framework but encompass distinct amino acid residues in the β_1 and β_2 portions, exhibited different aggregation dynamics, with distinguishable kinetic parameters (Fig. 6h and Supplementary Table 1), and ability to lower $A\beta_{40}$-associated cytotoxicity (Fig. 6j and Supplementary Fig. 17). Specifically, M28 and M32, compared to ZF2', displayed longer $t_{1/2,1}$

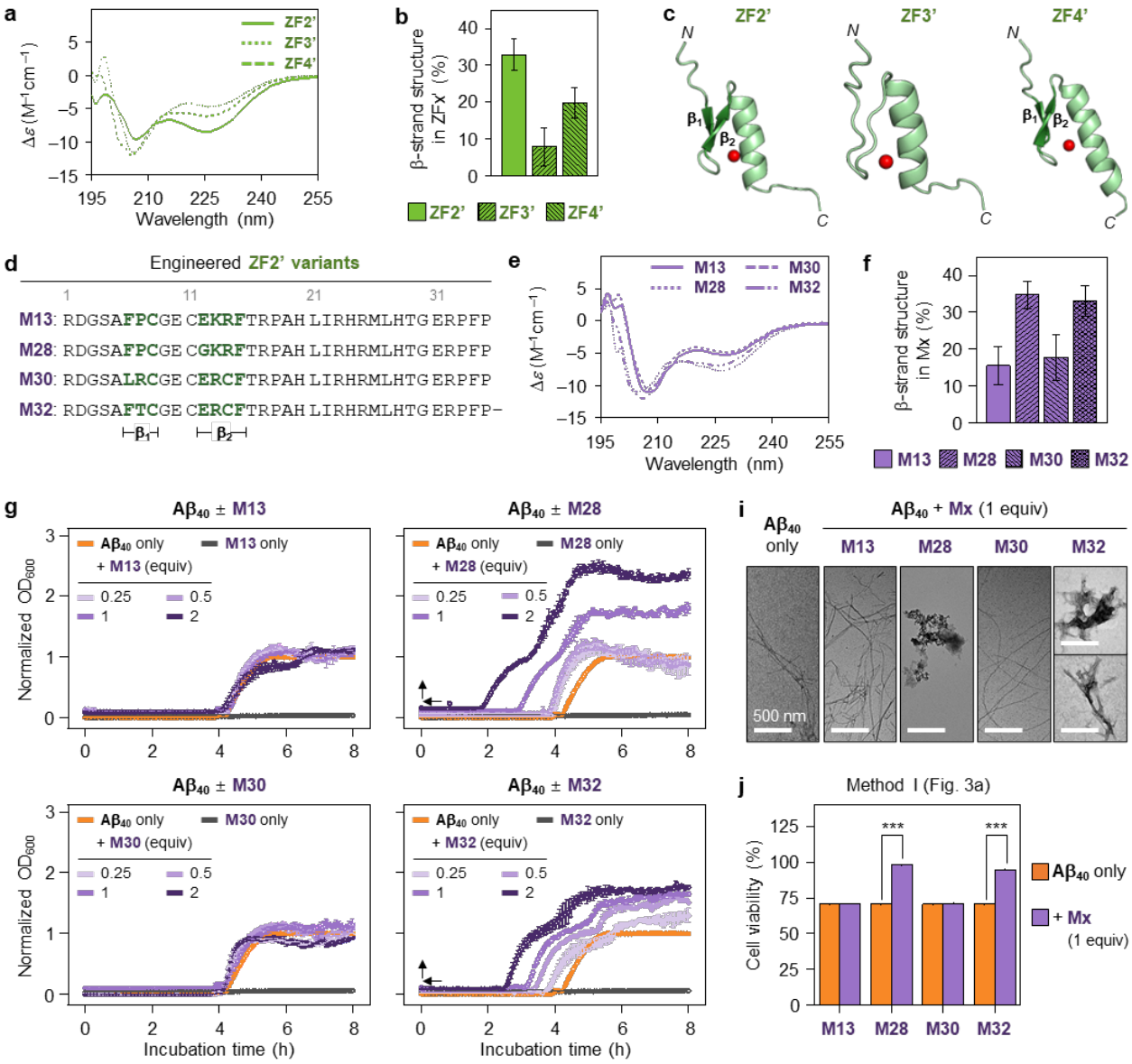

h

	Aβ40 only	+ ZF2' (1 equiv)	+ M13 (1 equiv)	+ M28 (1 equiv)	+ M30 (1 equiv)	+ M32 (1 equiv)
$t_{1/2,1}$ (h)	4.68 (± 0.01)	1.81 (± 0.01)	4.66 (± 0.03)	3.26 (± 0.01)	4.51 (± 0.05)	3.45 (± 0.01)
$t_{1/2,2}$ (h)	*n.a.*	5.74 (± 0.02)	*n.a.*	4.38 (± 0.02)	*n.a.*	5.01 (± 0.03)
I_{max} / $I_{A\beta}$	1.00 (± 0.01)	2.82 (± 0.02)	0.86 (± 0.03)	1.25 (± 0.02)	0.88 (± 0.03)	1.14 (± 0.02)

Fig. 6 | Impact of ZF2' variants on Aβ40 aggregation and cytotoxicity. a,b, Secondary structures of ZF2', ZF3', and ZF4' [Zn(II)-bound form] analyzed by CD spectroscopy. The β-strand composition of ZF2', ZF3', and ZF4' from each CD spectrum was analyzed by BeStSel[50]. Conditions: [apo-ZFx'] = 100 μM; [Zn(II)] = 90 μM; 20 mM HEPES, pH 7.4, 150 mM NaF, 1 mM DTT. Note that 0.9 equiv of Zn(II) was added to apo-ZFx' and incubated for 3 min to avoid the

presence of free Zn(II). **c,** 3D structural modeling of ZF2', ZF3', and ZF4' predicted by AlphaFold2[41,42], followed by docking Zn(II). Note that AlphaFold2 modeled the structures of ZF proteins based on the database (their Zn(II)-bound forms). **d,** Amino acid sequences of rationally selected M13, M28, M30, and M32. Amino acid residues in the β-hairpin regions are highlighted in bold and green. **e,f,** Secondary structures of M13, M28, M30, and M32 [Zn(II)-bound form] analyzed by CD spectroscopy. The β-strand composition of Mx from each CD spectrum was analyzed by BeStSel[50]. Conditions: [apo-Mx] = 100 μM; [Zn(II)] = 90 μM; 20 mM HEPES, pH 7.4, 150 mM NaF, 1 mM DTT. **g,h,** Aggregation kinetics of $A\beta_{40}$ with and without selected ZF2' variants [Mx; Zn(II)-bound form] monitored by the turbidity assay. The kinetic parameters of $A\beta_{40}$ incubated with and without ZF2' or Mx were obtained by fitting the absorbance curves using the modified Boltzmann-sigmoidal or double Boltzmann-sigmoidal equations. *n.a.* not available. Note that the $t_{1/2,2}$ value of $A\beta_{40}$ aggregation showing a monophasic growth is not defined. Conditions: [$A\beta_{40}$] = 100 μM; [apo-Mx] = 25, 50, 100, and 200 μM; [Zn(II)] = 22.5, 45, 90, and 180 μM; 20 mM HEPES, pH 7.4, 150 mM NaCl, 1 mM DTT; 37 °C; quiescence; λ_{abs} = 600 nm. Data are presented as mean ± s.e.m. of three independent experiments. **i,** Morphologies of the resultant aggregates by incubation of $A\beta_{40}$ with and without Mx for 8 h monitored by TEM. Conditions: [$A\beta_{40}$] = 100 μM; [apo-Mx] = 100 μM; [Zn(II)] = 90 μM; 20 mM HEPES, pH 7.4, 150 mM NaCl, 1 mM DTT; 37 °C; quiescence. Scale bar = 500 nm. **j,** Viability of the cells treated with $A\beta_{40}$ incubated with and without Mx determined by the MTT assay. Cell survival was calculated in comparison to that with an equivalent amount of the buffered solution. Conditions: [$A\beta_{40}$] = 10 μM; [apo-Mx] = 10 μM; [Zn(II)] = 9 μM; 20 mM HEPES, pH 7.4, 150 mM NaCl; 8 h pre- and 48 h post-incubation; 37 °C; quiescence; SH-SY5Y cells that were non-differentiated. ***$P < 0.001$; n = 3; Student's *t*-test. Data are presented as mean ± s.e.m.

values of $A\beta_{40}$ aggregation with reduced formation of $A\beta_{40}$ aggregates. These results support the role of the components composing the β-hairpin structure, in addition to its mere existence, in redirecting the on-pathway toxic $A\beta_{40}$ amyloidogenesis into less toxic amorphous aggregation. Taken together, our investigations into the sequence–reactivity relationship confirmed specific structural determinants, particularly the ZF2 and ZF4 domains, as responsible for directing PARIS(ZF2–4)'s modulative reactivity towards $A\beta_{40}$ aggregation and cytotoxicity, with an emphasis on the critical role of the ZF2 framework.

Conclusion

While the involvement of PARIS in inducing mitochondrial dysfunction and oxidative stress through PGC-1α downregulation has been established under Parkin-inactivated conditions[15,16], its broader functions remain largely unexplored. Given that PARIS(ZF2–4) comprises three classical ZF structural motifs crucial for PARIS's binding to Parkin and PGC-1α[14,16], we investigated its capability to interact directly with amyloidogenic proteins, potentially impacting disease progression. Our studies uncover the direct binding of PARIS(ZF2–4) to Aβ and its modulatory reactivity towards the aggregation and cytotoxicity of Aβ, providing mechanistic insights based on the detailed sequence-based reactivity analysis.

PARIS(ZF2–4) forms a complex with $A\beta_{40}$ with a sub-micromolar binding affinity through direct contacts onto key regions accountable for Aβ aggregation, which is predicted to alter the aggregation and cytotoxicity profiles of Aβ[26,27]. Through their complexation, PARIS(ZF2–4) promotes the amorphous aggregation of $A\beta_{40}$, and similar reactivity is shown with $A\beta_{42}$. In the presence of PARIS(ZF2–4), the interaction between $A\beta_{40}$ species and cellular membranes is reduced, accompanied by decreased formation of toxic oligomeric and fibrillar aggregates, resulting in diminished cytotoxicity. Our spectroscopic and computational analyses indicate that direct binding of the ZF2 and ZF4 regions from PARIS(ZF2–4) to $A\beta_{40}$ induces structural changes in both proteins, reshaping $A\beta_{40}$ aggregation dynamics while maintaining binding. Furthermore, our comprehensive sequence–reactivity relationship investigations pinpoint the pivotal roles of the ZF2 and ZF4 domains in accelerating the production of less toxic amorphous $A\beta_{40}$ aggregates, emphasizing the importance of the β-hairpin structure within the ZF domains. These findings offer novel insights into the multifaceted functions of PARIS(ZF2–4) in neurodegenerative disorders and underscore specific structural motifs dictating its modulative reactivity against Aβ amyloidogenesis.

Having identified PARIS(ZF2–4), ZF2', ZF4', M28, and M32 as possessing a β-hairpin structure capable of redirecting freshly prepared $A\beta_{40}$ into amorphous aggregation, we further probed their ability to disassemble preformed $A\beta_{40}$ aggregates or modulate their further aggregation. As illustrated in Supplementary Figs. 18 and 19, highly branched mature fibrils observed in preformed $A\beta_{40}$ aggregates were disassembled into short and thin chopped fibrils as well as amorphous aggregates upon treatment with PARIS(ZF2–4) and its variants harboring β-hairpin motifs. Therefore, the ZF proteins, with β-hairpin structures, studied in this work show the noticeable impact on redirecting both the formation of $A\beta_{40}$ aggregates and the presence of its

preformed aggregates. Of particular interest, ZF2' and its engineered variants exhibit noticeable reactivity towards $A\beta_{40}$ in our aggregation and cell experiments, suggesting the potential of ZF2' as a promising platform for developing peptide-based drugs against Aβ amyloidogenesis. In the near future, we aim to design ZF2'-based drug candidates for AD, considering properties for bioavailability, such as metabolic stability and blood-brain barrier permeability. Overall, this work is the first report to describe the direct binding of ZF proteins with Aβ, with the consequent impact on its aggregation and cytotoxicity behaviors. Our study demonstrates that PARIS(ZF2–4) and its fragments or variants can reprofile the aggregation and cytotoxicity of Aβ through their direct binding and subsequent conformational changes, emphasizing a new modulative function of ZF proteins against Aβ amyloidogenesis.

Methods

Materials and methods. All chemical reagents were purchased from commercial suppliers and used as received unless otherwise stated. PARIS(ZF2–4) (MGSALRCGECGRCFTRPAHLIRH-RMLHTGERPFPCTECEKRFTERSKLIDHYRTHTGVRPFTCTVCGKSFIRKDHLRKHQRNHAAG AK) was recombinantly expressed in *E. coli* and purified as previously reported[16]. $A\beta_{40}$ (DAEFR-HDSGYEVHHQKLVFFAEDVGSNKGAIIGLMVGGVV) and $A\beta_{42}$ (DAEFRHDSGYEVHHQKLVFF-AEDVGSNKGAIIGLMVGGVVIA) were obtained from Peptide Institute, Inc. (Osaka, Japan) that was purified by high-performance liquid chromatography using YMC Pack ODS-A (YMC CO., LTD., Kyoto, Japan) and Agilent ZORBAX 300SB-C18 columns (Agilent, Santa Clara, CA, USA). $^{HF488}A\beta_{40}$ and uniformly ^{15}N-labeled $A\beta_{40}$ were purchased from AnaSpec (Fremont, CA, USA) and rPeptide Inc. (Bogart, GA, USA), respectively. PARIS(ZF2–4) fragments and ZF2' variants (ZF2', RDGSALRCGECGRCFTRPAHLIRHRMLHTGERPFP; ZF3', TGERPFPCTECEKRFTERSKLID-HYRTHTGVRPFT; ZF4', TGVRPFTCTVCGKSFIRKDHLRKHQRNHAAGAKTP; M13, RDGSAF-PCGECEKRFTRPAHLIRHRMLHTGERPFP; M28, RDGSAFPCGECGKRFTRPAHLIRHRMLHT-GERPFP; M30, RDGSALRCGECERCFTRPAHLIRHRMLHTGERPFP; M32, RDGSAFTCGECE-RCFTRPAHLIRHRMLHTGERPFP) were obtained from Anygen (Gwangju, Republic of Korea). HEPES [2-(4-(2-hydroxyethyl)piperazin-1-yl)ethanesulfonic acid] and MOPS [3-(*N*-morpholino)propanesulfonic acid] were purchased from Sigma-Aldrich (St. Louis, MO, USA). The buffered solution was prepared in doubly distilled water [ddH_2O; a Milli-Q Direct 16 system (18.2 MΩ·cm; Merck KGaA, Darmstadt, Germany)]. Trace metal contamination was removed from all solutions used for experiments by treating with Chelex (Sigma-Aldrich) overnight. The concentrations of peptides were determined by an Agilent 8453 ultraviolet−visible

spectrophotometer (Agilent). The concentration of zinc in prepared PARIS(ZF2–4) was measured by an Agilent ICP–MS 7700S [Agilent; KAIST Analysis Center for Research Advancement (KARA), Daejeon, Republic of Korea]. The fluorescence spectra were recorded on a FP-8300 spectrofluorometer (JASCO Inc., Tokyo, Japan). The absorbance and fluorescence values were determined by a SpectraMax M5 microplate reader (Molecular Devices, Sunnyvale, CA, USA) and a HORIBA QuantaMaster QM 400 spectrophotometer (HORIBA, Kyoto, Japan; KARA). 2D ^{1}H–^{15}N HMQC or HSQC NMR spectroscopy was conducted by an AVANCE II-800 MHz NMR spectrometer [Bruker BioSpin, Rheinstetten, Germany; Korea Basic Science Institute (KBSI), Ochang, Republic of Korea] equipped with a cryogenic probe. Images gained through gel/Western blot were visualized by a ChemiDoc MP imaging system (Bio-Rad, Hercules, CA, USA). Morphologies of Aβ aggregates produced from aggregation experiments were taken on a Tecnai F20 transmission electron microscope (FEI Company, Eindhoven, Netherlands; KARA). The secondary structures of samples were analyzed by a JASCO-815 150-L CD spectropolarimeter (JASCO Inc.). Live-cell microinjection experiments were performed by the combined system composed of an InjectMan 4 micromanipulator (Eppendorf, Hamburg, Germany) and a Femtojet 4i microinjector (Eppendorf). Fluorescence analysis of living cells was conducted by an EVOS FL fluorescence microscope (Advanced Microscopy Group, Bothell, WA, USA). Confocal microscopic images were taken by a Zeiss LSM 880 (Carl ZEISS, Oberkochen, Germany; KARA). Detailed experimental procedures are described in the Supplementary Information.

Acknowledgments

This work was supported by the National Research Foundation of Korea (NRF) grant funded by the Korean government [NRF-2022R1A3B1077319 (M.H.L.); NRF-2019R1A2C1004954 and NRF-2022R1A2C1011793 (Y.-H.L.)]; the Ministry of Education [NRF-2017R1A6A1A03015876 (S.J.L.)]; the Institute for Basic Science (IBS-R010-A1) in Korea (J.P.); National Research Council of Science & Technology (NST) grant funded by the Korean government [CCL22061-100 (Y.-H.L.)]; KBSI fund [C320000, C330130, C390000, and C318410 (Y.-H.L.)].

Author contributions

S.P., S.J.L., and M.H.L. designed the research. S.P. performed spectroscopic measurements (absorbance, fluorescence, and CD), PAGE, biochemical assays, ICC studies, protein–protein docking studies, and AlphaFold2 modeling with data analysis. Y.H., H.G.K., and S.J.L. conducted the expression and purification of PARIS(ZF2–4), ^{15}N-labeled PARIS(ZF2–4), and ^{HF555}PARIS(ZF2–4). Y.L. and Y.-H.L. conducted 2D ^{1}H–^{15}N HMQC NMR experiments and

analyzed the data. J.P. carried out MD simulations with analysis. J.K. and S.P. carried out TEM measurements. E.N., J.H., and S.P. performed live-cell studies. S.P., J.P., and M.H.L. wrote the manuscript with input from all authors.

Competing financial interests. The authors declare no competing financial interests.

References

1. Fu, M. & Blackshear, P. J. RNA-binding proteins in immune regulation: a focus on CCCH zinc finger proteins. *Nat. Rev. Immunol.* **17**, 130–143 (2017).
2. Jamieson, A. C., Miller, J. C. & Pabo, C. O. Drug discovery with engineered zinc-finger proteins. *Nat. Rev. Drug Discov.* **2**, 361–368 (2003).
3. Gao, G., Guo, X. & Goff, S. P. Inhibition of retroviral RNA production by ZAP, a CCCH-type zinc finger protein. *Science* **297**, 1703–1706 (2002).
4. Lee, S. J. & Michel, S. L. J. Structural metal sites in nonclassical zinc finger proteins involved in transcriptional and translational regulation. *Acc. Chem. Res.* **47**, 2643–2650 (2014).
5. Cassandri, M. *et al.* Zinc-finger proteins in health and disease. *Cell Death Discov.* **3**, 17071 (2017).
6. Bu, S., Lv, Y., Liu, Y., Qiao, S. & Wang, H. Zinc finger proteins in neuro-related diseases progression. *Front. Neurosci.* **15**, 760567 (2021).
7. Al-Naama, N., Mackeh, R. & Kino, T. C_2H_2-type zinc finger proteins in brain development, neurodevelopmental, and other neuropsychiatric disorders: systematic literature-based analysis. *Front. Neurol*. **11**, 32 (2020).
8. Meng, X., Noyes, M. B., Zhu, L. J., Lawson, N. D. & Wolfe, S. A. Targeted gene inactivation in zebrafish using engineered zinc-finger nucleases. *Nat. Biotechnol.* **26**, 695–701 (2008).
9. Monteferrario, D. *et al.* Epigenetic control of multiple genes with a lentiviral vector encoding transcriptional repressors fused to compact zinc finger arrays. *Mol. Ther. Methods Clin. Dev.* **32**, 101255 (2024).
10. Wegmann, S. *et al.* Persistent repression of tau in the brain using engineered zinc finger protein transcription factors. *Sci. Adv.* **7**, eabe1611 (2021).
11. Li, X. *et al.* Structures and biological functions of zinc finger proteins and their roles in hepatocellular carcinoma. *Biomark. Res.* **10**, 2 (2022).
12. Ichikawa, D. M. *et al*. A universal deep-learning model for zinc finger design enables

transcription factor reprogramming. *Nat. Biotechnol.* **41**, 1117–1129 (2023).

13. Savelieff, M. G., Nam, G., Kang, J., Lee, H. J., Lee, M. & Lim, M. H. Development of multifunctional molecules as potential therapeutic candidates for Alzheimer's disease, Parkinson's disease, and amyotrophic lateral sclerosis in the last decade. *Chem. Rev.* **119**, 1221–1322 (2019).
14. Shin, J. H. *et al*. PARIS (ZNF746) repression of PGC-1α contributes to neurodegeneration in Parkinson's disease. *Cell* **144**, 689–702 (2011).
15. Brahmachari, S. *et al*. Parkin interacting substrate zinc finger protein 746 is a pathological mediator in Parkinson's disease. *Brain* **142**, 2380–2401 (2019).
16. Hwang, Y. *et al*. Decoding the Parkinson's symphony: PARIS, maestro of transcriptional regulation and metal coordination for dopamine release. *ACS Chem. Neurosci.* **15**, 447–455 (2024).
17. St-Pierre, J. *et al*. Suppression of reactive oxygen species and neurodegeneration by the PGC-1α transcriptional coactivators. *Cell* **127**, 397–408 (2006).
18. Brayer, K. J. & Segal, D. J. Keep your fingers off my DNA: protein–protein interactions mediated by C_2H_2 zinc finger domains. *Cell Biochem. Biophys.* **50**, 111–131 (2008).
19. Rosen, K. M. *et al*. Parkin reverses intracellular β-amyloid accumulation and its negative effects on proteasome function. *J. Neurosci. Res*. **88**, 167–178 (2010).
20. Han, J., Du, Z. & Lim, M. H. Mechanistic insight into the design of chemical tools to control multiple pathogenic features in Alzheimer's disease. *Acc. Chem. Res.* **54**, 3930–3940 (2021).
21. Benilova, I., Karran, E. & De Strooper, B. The toxic Aβ oligomer and Alzheimer's disease: an emperor in need of clothes. *Nat. Neurosci.* **15**, 349–357 (2012).
22. Kayed, R. *et al*. Common structure of soluble amyloid oligomers implies common mechanism of pathogenesis. *Science* **300**, 486–489 (2003).
23. Lin, Y. *et al*. Diverse structural conversion and aggregation pathways of Alzheimer's amyloid-β (1-40). *ACS Nano* **13**, 8766–8783 (2019).
24. Yoo, J. M., Lin, Y., Heo, Y. & Lee, Y.-H. Polymorphism in α-synuclein oligomers and its implications in toxicity under disease conditions. *Front. Mol. Biosci.* **9**, 959425 (2022).
25. Park, S., Na, C., Han, J. & Lim, M. H. Methods for analyzing the coordination and aggregation of metal–amyloid-β. *Metallomics* **15**, mfac102 (2023).
26. Kim, Y.-M. *et al*. Clusterin binding modulates the aggregation and neurotoxicity of amyloid-β(1–42). *Mol. Neurobiol.* **59**, 6228–6244 (2022).

27. Taş, K. *et al.* Designed peptides as nanomolar cross-amyloid inhibitors acting via supramolecular nanofiber co-assembly. *Nat. Commun.* **13**, 5004 (2022).
28. Lin, Y. *et al*. An amphiphilic material arginine–arginine–bile acid promotes α-synuclein amyloid formation. *Nanoscale* **15**, 9315–9328 (2023).
29. Lin, Y. *et al*. Dual effects of presynaptic membrane mimetics on α-synuclein amyloid aggregation. *Front. Cell Dev. Biol*. **10**, 707417 (2022).
30. Yoshimura, Y. *et al*. Distinguishing crystal-like amyloid fibrils and glass-like amorphous aggregates from their kinetics of formation. *Proc. Natl. Acad. Sci. U. S. A.* **109**, 14446–14451 (2012).
31. Bernstein, S. L. *et al*. Amyloid-β protein oligomerization and the importance of tetramers and dodecamers in the aetiology of Alzheimer's disease. *Nat. Chem.* **1**, 326–331 (2009).
32. Ehrnhoefer, D. E. *et al*. EGCG redirects amyloidogenic polypeptides into unstructured, off-pathway oligomers. *Nat. Struct. Mol. Biol.* **15**, 558–566 (2008).
33. Kuramochi, M. *et al*. Adenosine triphosphate induces amorphous aggregation of amyloid β by increasing Aβ dynamics. *Sci. Rep.* **14**, 8134 (2024).
34. Du, Z. *et al*. Unveiling the impact of oxidation-driven endogenous protein interactions on the dynamics of amyloid-β aggregation and toxicity. *Chem. Sci*. **14**, 5340–5349 (2023).
35. Han, J. *et al*. Conformational and functional changes of the native neuropeptide somatostatin occur in the presence of copper and amyloid-β. *Nat. Chem.* **14**, 1021–1030 (2022).
36. Nam, E. *et al*. APP-C31: an intracellular promoter of both metal-free and metal-bound amyloid-β_{40} aggregation and toxicity in Alzheimer's disease. *Adv. Sci.* **11**, 2307182 (2024).
37. Urbanc, B. *et al*. Neurotoxic effects of thioflavin S-positive amyloid deposits in transgenic mice and Alzheimer's disease. *Proc. Natl. Acad. Sci. U. S. A.* **99**, 13990–13995 (2002).
38. Tsai, J., Grutzendler, J., Duff, K. & Gan, W.-B. Fibrillar amyloid deposition leads to local synaptic abnormalities and breakage of neuronal branches. *Nat. Neurosci.* **7**, 1181–1183 (2004).
39. Lu, J.-X. *et al*. Molecular structure of β-amyloid fibrils in Alzheimer's disease brain tissue. *Cell* **154**, 1257–1268 (2013).
40. Ha, S. H. & Ferrell Jr., J. E. Thresholds and ultrasensitivity from negative cooperativity. *Science* **352**, 990–993 (2016).
41. Jumper, J. *et al*. Highly accurate protein structure prediction with AlphaFold. *Nature* **596**, 583–589 (2021).

42. Mirdita, M. *et al*. ColabFold: making protein folding accessible to all. *Nat. Methods* **19**, 679–682 (2022).
43. Vivekanandan, S., Brender, J. R., Lee, S. Y. & Ramamoorthy, A. A partially folded structure of amyloid-β(1-40) in an aqueous environment. *Biochem. Biophys. Res. Commun.* **411**, 312–316 (2011).
44. Kozakov, D. *et al*. The ClusPro web server for protein–protein docking. *Nat. Protoc.* **12**, 255–278 (2017).
45. Case, D. A. *et al*. The Amber biomolecular simulation programs. *J. Comput. Chem.* **26**, 1668–1688 (2005).
46. Kollman, P. A. *et al*. Calculating structures and free energies of complex molecules: combining molecular mechanics and continuum models. *Acc. Chem. Res.* **33**, 889–897 (2000).
47. Govind Kumar, V., Polasa, A., Agrawal, S., Kumar, T. K. S. & Moradi, M. Binding affinity estimation from restrained umbrella sampling simulations. *Nat. Comput. Sci.* **3**, 59–70 (2023).
48. Gohlke, H. & Case, D. A. Converging free energy estimates: MM-PB(GB)SA studies on the protein–protein complex Ras–Raf. *J. Comput. Chem.* **25**, 238–250 (2004).
49. Stefaniak, E. *et al*. The aggregation pattern of $A\beta_{1\text{-}40}$ is altered by the presence of *N*-truncated $A\beta_{4\text{-}40}$ and/or Cu^{II} in a similar way through ionic interactions. *Chem. Eur. J.* **27**, 2798–2809 (2021).
50. Micsonai, A. *et al*. BeStSel: webserver for secondary structure and fold prediction for protein CD spectroscopy. *Nucleic Acids Res.* **50**, W90–W98 (2022).